From double to triple porosity modelling of bentonite pellet mixtures

Preprint form of the journal article published in Engineering Geology, https://doi.org/10.1016/j.enggeo.2020.105714. This version does not include the peer-review, copyediting and typesetting changes included in its published form.

Vicente Navarro [a*], Laura Asensio [a], Gema De la Morena [a], Heidar Gharbieh [b], Juan Alonso [a], Veli-Matti Pulkkanen [b]

[a] Geoenvironmental Group, Universidad de Castilla-La Mancha. Avda. Camilo José Cela s/n, 13071 Ciudad Real, Spain.

[b] VTT Technical Research Centre of Finland Ltd. P.O. Box 1000, FI-02044 VTT, Finland.

*: Corresponding author: Vicente Navarro. Tel.: +34 926295300. Email: vicente.navarro@uclm.es.

E-mail addresses: vicente.navarro@uclm.es (V. Navarro), laura.asensio@uclm.es (L. Asensio), gema.delamorena@uclm.es (G. De la Morena), heidar.gharbieh@vtt.fi (H. Gharbieh), juan.alonso@uclm.es (J. Alonso), veli-matti.pulkkanen@vtt.fi (V.M. Pulkkanen)

Abstract

The present work analyses the hydro-mechanical behaviour of bentonite pellet mixtures using a macroscopic overlapping continua approach based on a triple porosity model. Two macrostructural functional levels are considered (inter-pellet pore space and void space between the clay aggregates inside the pellets) as well as a microstructural level (related to the space inside the aggregates). This triple porosity approach reveals that, when assuming a double porosity model, the intrinsic permeability, tortuosity and degree of saturation of the single macrostructural level under consideration are the average values of the state functions of the adopted triple porosity model, but are not state functions themselves.

The analysis also illustrates that, when assuming the same liquid pressure for the two macrostructural levels of the triple porosity model, it is relatively easy to expand upon the calculation procedures initially developed for a double porosity model to include a triple porosity model.

When evaluating the applicability of the model, quality results were obtained, comparable to those of a triple porosity model, for both open and closed bentonite pellet mixtures. The results are better than those obtained with a double porosity model, since the state functions have a stronger physic base when using a triple porosity approach. Encouraging results are also obtained when analysing the overall swelling of a bentonite block and a mixture of bentonite pellets, using the same parameters for both materials. Therefore, given its capacity for relatively simple incorporation in a double porosity models, the model offers an interesting tool for researchers working on improving the characterisation of bentonite pellet mixtures.

Keywords

Bentonite pellet mixtures, bentonite, hydro-mechanical model, pellets triple porosity model, double porosity model, high-level radioactive waste.

1. Introduction

Bentonite pellet mixtures (BPM) are considered as components of the engineered barrier systems included in distinct repository concepts for the disposal of high-level radioactive waste (Sellin and Leupin, 2013). Therefore, based on intensive experimental work (Hoffmann et al., 2007; Imbert and Villar 2006; Karnland et al. 2008; García-Siñeriz et al. 2015; Molinero Guerra et al. 2018, 2019), a major effort is being made to define its Thermo-Hydro-Mechanical-Chemical (THMC) behaviour.

Interesting results were obtained using a double porosity approach (Alonso et al., 2011; Gens et al., 2011; Sánchez et al., 2016), adopting the reference framework provided by macroscopic models simulating the behaviour of compacted bentonite blocks (Gens and Alonso, 1992; Guimarães et al., 2013; Nowamooz et al. 2009; Sánchez et al., 2005; Vilarrasa et al., 2016). In blocks, the overlapping continua approach introduced by Barenblatt et al. (1960) for fissured rock is usually assumed, expanded, among others by Khalili et al. (1999) and Wilson and Aifantis (1982) for soils. In this approach, the behaviour of the system is characterised by two distinct continuous media that interact, occupying the same spatial domain. One of the continua, the "microstructure", is the tool that permits the description of the macroscopic effect of the voids in which the hydrodynamic flow is almost negligible. This restrictive definition (voids with no hydrodynamic flow) implies that, despite its functional definition, the microstructural functional level has a specific structural support, being fundamentally associated with the intra-aggregated void space. The other continuous medium, the macrostructure, introduces the macroscopic effect of the remainder of the porous medium. In "as compacted" conditions, with a marked bimodal pore size distribution (see Lloret et al., 2003, for instance), the "macro" functional level may be associated with a specific pore size. However, this is not the case when the bimodal structure evolves as the load,

saturation or salinity conditions change (Musso et al., 2003; Lloret and Villar, 2007; Manca et al., 2016; Bian et al., 2019). Nevertheless, this loss of structural reference has not compromised the utility of double porosity models (DPMs), which have successfully characterised the THMC behaviour of bentonite blocks under a wide range of conditions (Guimarães et al., 2013; Mašín, 2013; Navarro et al., 2017; Nowamooz et al., 2009; Sánchez et al., 2005; Vilarrasa et al., 2016).

However, it is not clear that this abstraction capacity will be held in BPM, with a multi-modal pore structure having much larger pores than those existing in a compacted bentonite block (see Fig. 1). Therefore, Navarro et al. (2019) proposed the application of a triple porosity model to characterise the hydro-mechanical behaviour of BPM ("PTPM" model, Pellets Triple Porosity Model). In that proposal, the definition of the microstructural functional level (identified as "*m*") was maintained as the porosity without hydrodynamic flow (having a void ratio e_m, defined as the volume of intra-aggregate voids per volume of mineral). However, two functional levels were differentiated in the macrostructure. The first (level "*M*1", with a void ratio e_{M1}) introduces the macroscopic effect of the intra-pellet inter-aggregate voids in the model. The second (level "*M*2", void ratio e_{M2}) simulates the effect of the largest voids, associated with the inter-pellet void space, on a macroscopic scale. The PTPM reveals that, since they do not simulate the evolution of e_{M2}, DPMs have certain difficulties in reproducing the variation of the behaviour of the system if the confinement does not ensure a fast reduction of this void space. Therefore, if a DPM is used to reproduce a test in which e_{M2} is relevant, at times, the value of the material parameters is forced, projecting the responsibility of characterising the evolution of the mixture on them. In this case, the parameters of the models are fitting parameters more than material parameters.

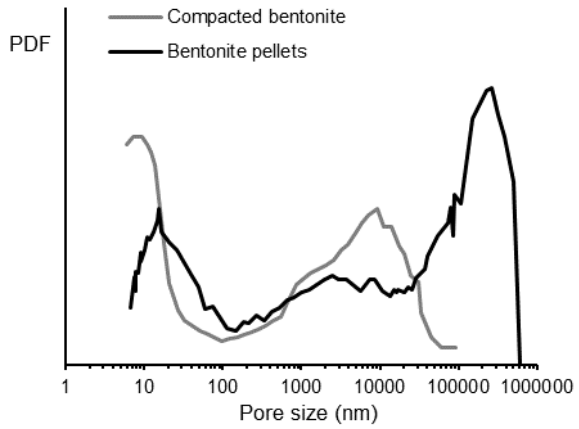

Fig. 1. Pore size distributions obtained with mercury intrusion porosimetry of a compacted bentonite sample (dry density 1800 kg/m^3; adapted from Lloret et al., 2003), and a bentonite pellet sample (prepared using gravity fall compaction, overall dry density of 1150 kg/m^3; adapted from Hoffmann et al., 2007). (PDF: Pore Distribution Frequency).

The objective of the present paper is to analyse this projection, using the conceptual framework provided by the PTPM as a reference. With this analysis, focused on hydro-mechanical (HM) behaviour, the aim is to evaluate the possibility of adopting an alternative HM approach, in which the calculation procedures that are normally used in double porosity models may be applied, incorporating an idealisation of the system based on a triple porosity model (in which the evolution of e_{M2} is taken into account). Afterwards, once the conceptual framework is defined, its scope and limitations are evaluated by simulating the three hydration tests described in the following section.

2. Material and methods

The first test analysed was carried out by CEA (France) (Bernachy-Barbe et al., in prep.) (Test 1), while the second was carried out by Clay Technology (Sweden) (Åkesson et al., in prep.) (Test 2). In both cases, MX-80 bentonites with 80%

montmorillonite were used, although from different suppliers. The material used in Test 1 was described in detail by Molinero Guerra et al. (2017), while Karnland et al. (2006) provided an extensive description of the material used in Test 2. In both cases, the main exchangeable cations were Na^+ (55 meq/100g, Test 1, and 52 meq/100g, Test 2), and Ca^{2+} (37 meq/100g, Test 1, and 12 meq/100g, Test 2), with cation exchange capacities of the bentonite being 75 meq/100g and 98 meq/100g, respectively. The mineral density of both materials was practically the same (2770 kg/m^3, Test 1, and 2780 kg/m^3, Test 2). In Test 1, pellets with a cylindrical side shape finished in two semi-spheres were used. The pellets, with a maximum dimension of 32 mm, were manufactured by compacting bentonite powder in a mould (Molinero Guerra et al., 2017) to a dry density of between 2010 and 2050 kg/m^3, and a water content of 4%. Poured alternatively in layers, the sample mass was 70 % intact pellets and 30% crushed pellets, with a particle size of less than 2.5 mm. In Test 2, intact pillow-shaped pellets with a maximum dimension of 16 mm were used (Luterkort et al., 2017). The pellets, having a water content of 15%, were produced by compaction between two rollers to a dry density of 1841 kg/m^3.

In both tests, cylindrical samples were tested, with a diameter of 240 m and a height of 101.15 mm in Test 1, and a diameter of 100 mm and height of 500 mm in Test 2. The samples were kept confined, hydrating them from the bottom by applying water at a pressure of 10 kPa (Test 1) and 1 kPa (Test 2) for 940 and 200 days, respectively.

Test 3 was carried out by Posiva (Talandier, 2018). In this test, also conducted in confined conditions, a cylindrical sample of 100 mm in diameter and height was hydrated from its upper face. The lower part of the sample (up to 48.5 mm in height) was formed by a clay block compacted directly into the cell, having initial dry density and water content values of 1808 kg/m^3 and 16.3%, respectively. The material, MX-80 bentonite, identified as Be-Wy--VT0002_BT by Kiviranta and Kumpulainen (2011),

contained 88% smectite. Its cation exchange capacity was 86 meq/100g, with Na^+ (58 meq/100g) and Ca^{2+} (24 meq/100g) being its main exchangeable cations. Its mineral density was equal to 2781 kg/m^3. The remainder of the sample was filled with pillow-shaped pellets sieved down to a minimum pellet size of 8 mm (pellet dimensions varied from 11.2 to 26.2 mm in length, from 10.3 to 14.7 mm in width, and from 5.4 to 5.9 mm in thickness). The individual pellets had an initial bulk density and water content of 2100 kg/m^3 and 15.3%, respectively. The average dry density of the pellet fill was equal to 904 kg/m^3. The pellets were manufactured using MX-80 bentonite, Be-Wy--BT0020-3-5a-R in Kiviranta et al. (2018), with 86% montmorillonite and a cation exchange capacity of 94 meq/100g. Their main exchangeable cations were Na^+ (63 meq/100g) and Ca^{2+} (18 meq/100g), with a mineral density of 2780 kg/m^3.

3. Conceptual framework. HM behaviour

3.1 Reference PTPM

As a reference approach of the multi-model pore structure of BPM, the PTPM proposed by Navarro et al. (2019) was adopted. It assumes a hierarchical interaction between the three functional levels considered. Thus, although the exchange of water mass between *M*2 and *M*1, $r_{\text{M2-M1}}$, was taken into account, the direct exchange between *M*2 and *m* is considered null. However, the exchange between *M*1 and *m*, $r_{\text{M1-m}}$, is considered. Therefore, *M*1 plays a role of interface, since it exchanges mass with *M*2 and *m*. The water mass balances in the three functional levels are written as follows:

[1] $$\frac{\partial m_{\text{M2}}}{\partial t} + \nabla \cdot \mathbf{l}_{\text{M2}} = -r_{\text{M2-M1}}$$

[2] $$\frac{\partial m_{\text{M1}}}{\partial t} + \nabla \cdot \mathbf{l}_{\text{M1}} = r_{\text{M2-M1}} - r_{\text{M1-m}}$$

[3] $$\frac{\partial m_{\text{m}}}{\partial t} + \nabla \cdot \mathbf{l}_{\text{m}} = r_{\text{M1-m}}$$

where "$\nabla\cdot$" is the divergence operator, and m_k is the water mass per total volume at each structural level "k" (*m*, *M*1 or *M*2) in which there is a mass flow rate $\mathbf{l}_k$ (vector or tensor magnitudes appear in bold throughout this paper). The water masses per total volume are calculated as follows:

$$[4] \qquad m_m = \rho_W \frac{e_m}{1+e}; \quad m_{Mi} = m_{Mi,L} + m_{Mi,V} = \rho_W \frac{e_{Mi}\, Sr_{Mi}}{1+e} + \rho_{V,Mi} \frac{e_{Mi}(1-Sr_{Mi})}{1+e}$$

where $m_{Mi,L}$ (i=1, 2) is the mass of liquid water in the macrostructural level *M*i per total volume, $m_{Mi,V}$ is the analogous magnitude in the vapour phase, ρ_W is the density of free water (assumed to equal 1000 kg/m^3 for the isothermal problems considered), Sr_{Mi} is the degree of saturation for water (volume of water per volume of voids in *M*i), *e* is the total void ratio (=e_m+e_{M1}+e_{M2}), and $\rho_{V,Mi}$ is the density of vapour in *M*i, calculated based on psychrometric law (Edlefsen and Anderson, 1943):

$$[5] \qquad \rho_{V,Mi} = \rho_{VO}(T) \exp\left(-\frac{WMM}{\rho_W R\, T} s_{Mi} \right)$$

where ρ_{VO} is the density of saturated water vapour at an absolute temperature *T*, *WMM* is the molar mass of water, *R* is the universal gas constant, and s_{Mi} defines the matric suction associated with each of the two structural levels (in the tests analysed, as a first approximation, the effect of the hydration water salinity is not considered). This latter is identified with the capillary suction s_{Mi}=P_G–P_{Li}, where P_{Li} is the liquid pressure in *M*i, and P_G is the gas pressure, equal to P_{atm} in the present paper.

In Eq. [4], the microstructural pores were considered to be saturated (see, for example, Gens and Alonso, 1992; Mašín and Khalili, 2016; Yong, 1999). In addition, as implicit in the functional definition of the microstructure, the water in *m* is assumed to be linked to the bentonite skeleton. Therefore, the microstructural mass flow rate is given by the expression:

$$[6] \qquad \mathbf{l}_m = m_m \mathbf{v}$$

where **v** is the solid skeleton velocity vector (time derivative of the displacement vector **u**). In *M*1 and *M*2 the water mass flow with respect to the bentonite skeleton is taken into account, defining the mass flow rate as:

[7] $$\mathbf{l}_{\mathrm{Mi}} = m_{\mathrm{Mi}}\mathbf{v} + \rho_{\mathrm{W}}\mathbf{q}_{\mathrm{Mi}} + \mathbf{j}_{\mathrm{Mi}}$$

where $\mathbf{q}_{\mathrm{Mi}}$ and $\mathbf{j}_{\mathrm{Mi}}$ are, respectively, the liquid specific discharge (or water seepage) and the vapour diffusion. Liquid water seepage is calculated in accordance with the generalised Darcy's law (Pollock, 1986):

[8] $$\mathbf{q}_{\mathrm{Mi}} = -\frac{k_{\mathrm{I,Mi}}\, k_{\mathrm{r,Mi}}}{\mu_{\mathrm{W}}}(\nabla P_{\mathrm{Li}} + \rho_{\mathrm{W}}\, g\, \nabla z)$$

where $k_{\mathrm{I,Mi}}$ and $k_{\mathrm{r,Mi}}$ are the intrinsic and the relative permeabilities of *M*i, respectively, μ_{W} is the liquid water dynamic viscosity, g is the gravitational acceleration, z defines the vertical coordinate oriented upwards, and "∇" expresses the gradient differential operator. Since gas pressure has been considered constant, the advective flow of the gas phase is assumed to be null, and hydrodynamic dispersion can be neglected. Therefore, vapour diffusion is identified with molecular diffusion, which is calculated in accordance with the generalised Fick's law, as:

[9] $$\mathbf{j}_{\mathrm{Mi}} = -\frac{\tau_{\mathrm{Mi}}\, e_{\mathrm{Mi}}(1 - Sr_{\mathrm{Mi}})\, D_{\mathrm{V}}\, \nabla \rho_{\mathrm{V,Mi}}}{1 + e}$$

where τ_{Mi} is the tortuosity to vapour flow, and D_{V} is the binary diffusion coefficient of water vapour in gas.

3.2 An inspection of DPMs using a PTPM as a reference

If a DPM is used to model the behaviour of BPM, the effect of *M*1 and *M*2 on the system is modelled using a single macrostructural functional level, "*M*", with a water mass per total volume, m_{M}, which integrates m_{M1} and m_{M2}. According to Eq. [4]:

[10] $$m_{\mathrm{M}} = m_{\mathrm{M1}} + m_{\mathrm{M2}} = \rho_{\mathrm{W}} \frac{\left(e_{\mathrm{M1}} Sr_{\mathrm{M1}} + e_{\mathrm{M2}} Sr_{\mathrm{M2}}\right)}{1+e} + \frac{\left(\rho_{\mathrm{V,M1}} e_{\mathrm{M1}}(1-Sr_{\mathrm{M1}}) + \rho_{\mathrm{V,M2}} e_{\mathrm{M2}}(1-Sr_{\mathrm{M2}})\right)}{1+e}$$

In the DPM, the value of m_{M} is calculated as:

[11] $$m_{\mathrm{M}} = m_{\mathrm{M,L}} + m_{\mathrm{M,V}} = \rho_{\mathrm{W}} \frac{e_{\mathrm{M}}\, Sr_{\mathrm{M}}}{1+e} + \rho_{\mathrm{V}} \frac{e_{\mathrm{M}}(1-Sr_{\mathrm{M}})}{1+e}$$

where ρ_{V} is the density of the water vapour in the macrostructure, e_{M} is the void ratio of *M*, which integrates e_{M1} and e_{M2} ($e_{\mathrm{M}}=e_{\mathrm{M1}}+e_{\mathrm{M2}}$). According to Eqs. [10] and [11], the degree of saturation of the macrostructure, Sr_{M}, should be:

[12] $$Sr_{\mathrm{M}} = \frac{\left(e_{\mathrm{M1}} Sr_{\mathrm{M1}} + e_{\mathrm{M2}} Sr_{\mathrm{M2}}\right)}{e_{\mathrm{M}}}$$

From which, using the PTPM as reference, a simple but important consequence is obtained: the Sr_{M} function used in a DPM is a weighted value of Sr_{M1} and Sr_{M2}, depending on e_{M1} and e_{M2}. Therefore, whether it is in fact a state function is questionable.

For mass transport, the mass flow rate associated with *M*, $\mathbf{l}_{\mathrm{M}}$, integrates $\mathbf{l}_{\mathrm{M1}}$ and $\mathbf{l}_{\mathrm{M2}}$. Therefore, according to Eqs. [7] and [10], it must be found that:

[13] $$\mathbf{l}_{\mathrm{M}} = \mathbf{l}_{\mathrm{M1}} + \mathbf{l}_{\mathrm{M2}} = m_{\mathrm{M}}\mathbf{v} + \rho_{\mathrm{W}}\left(\mathbf{q}_{\mathrm{M1}} + \mathbf{q}_{\mathrm{M2}}\right) + \mathbf{j}_{\mathrm{M1}} + \mathbf{j}_{\mathrm{M2}}$$

As in a DPM, the value of $\mathbf{l}_{\mathrm{M}}$ is obtained using an expression such as the following:

[14] $$\mathbf{l}_{\mathrm{M}} = m_{\mathrm{M}}\mathbf{v} + \rho_{\mathrm{W}}\ \mathbf{q}_{\mathrm{M}} + \mathbf{j}_{\mathrm{M}}$$

Where the liquid specific discharge, $\mathbf{q}_{\mathrm{M}}$, and the vapour diffusion, $\mathbf{j}_{\mathrm{M}}$, should be:

[15] $$\mathbf{q}_{\mathrm{M}} = \mathbf{q}_{\mathrm{M1}} + \mathbf{q}_{\mathrm{M2}}$$

[16] $$\mathbf{j}_{\mathrm{M}} = \mathbf{j}_{\mathrm{M1}} + \mathbf{j}_{\mathrm{M2}}$$

While a triple porosity model has two state variables associated with water flow, P_{L1} and P_{L2}, a DPM only has one, P_{L}, which defines the liquid water pressure in the macrostructure. Using the PTPM as reference, the conceptual consistency of P_{L} is

conditioned by the differences between P_{L1} and P_{L2}. In this work, cases in which *M*1 conditions the flow in the system are considered, with a slower kinetics than the exchange $r_{M2\text{-}M1}$, assuming the following:

[17] $$P_{L1} \approx P_{L2}$$

Therefore, if an equation such as Eq. [8] is used to calculate $\mathbf{q}_M$ in the DPM, it follows from Eq. [15] that the intrinsic and relative permeabilities of *M* ($k_{I,M}$ and $k_{r,M}$, respectively) are weighted values of those of *M*1 and *M*2:

[18] $$k_{I,M}\ k_{r,M} = k_{I,M1}\ k_{r,M1} + k_{I,M2}\ k_{r,M2}$$

If, as previously stated, the gas pressure is equal to the atmospheric pressure, the entire macrostructure has the same suction: $s_{M1}=s_{M2}$. Therefore, according to Eq. [5], $\rho_{V,M1}=\rho_{V,M2}$. Consequently, if $\mathbf{j}_M$ is calculated with Eq. [9], from Eq. [16] it follows that:

[19] $$\tau_M\ e_M(1-Sr_M) = \tau_{M1}\ e_{M1}(1-Sr_{M1}) + \tau_{M2}\ e_{M2}(1-Sr_{M2})$$

where τ_M is the tortuosity of *M*, weighted value of the tortuosities of *M*1 and *M*2.

3.3 A new triple-double porosity approach

Eqs. [12], [18] and [19] illustrate the main disadvantage of DPM: the degree of saturation, the permeability and tortuosity are not state functions, but rather, are weighted values of Sr_{M1}, Sr_{M2}, $k_{I,M1}$, $k_{I,M2}$, $k_{r,M1}$, $k_{r,M2}$, τ_{M1} and τ_{M2}. To work with state functions, it is convenient to use Eq. [10] instead of Eq. [11] to calculate the mass of water per total volume, and Eq. [13] instead of Eq. [14] to define the mass flow rate. This means recognising the differentiated existence of two macrostructural levels and, consequently, adopting a triple porosity conceptual framework.

However, even when *M*1 and *M*2 are differentiated, if Eq. [17] is assumed, the macrostructural water has only one degree of freedom, P_L, and, instead of Eqs. [1-2], only one water mass balance equation must be considered:

[20] $$\frac{\partial}{\partial t}\left(m_{M1}+m_{M2}\right)+\nabla\cdot\left(\mathbf{l}_{M1}+\mathbf{l}_{M2}\right)=-r_{M1\text{-}m}$$

Therefore, if m_M is changed by $m_{M1}+m_{M2}$ and $\mathbf{l}_M$ by $\mathbf{l}_{M1}+\mathbf{l}_{M2}$, the numerical tools developed to solve DPMs can be used to solve a model based on a triple porosity conceptual framework. The exchange term $r_{M1\text{-}m}$ can also be computed using the formulation in Navarro et al. (2015) for DPMs. Hence, it is suggested that this approach be identified as "D2TPM": Double to Triple Porosity Model.

There are two main difficulties in implementing this strategy. First, the evolution of the e_{M2} value must be defined, an important issue to be analysed in the following section. Second, it is necessary to incorporate more constitutive information than in a DPM, since the state functions Sr_{M2}, $k_{I,M2}$, and $k_{r,M2}$ must be defined. As an initial approximation to solve this problem, a simplified approach has been proposed. Due to the pellet size, it is expected that the value of the air-entry pressure in *M*2, $s_{A,M2}$, will be considerably low, and therefore both Sr_{M2} and $k_{r,M2}$ experience a sharp transition (almost a Heaviside step function) around this value. Therefore, a smoothed Heaviside function is adopted, assuming $s_{A,M2}$=0.5 kPa (Navarro et al., 2019). For $k_{I,M2}$, the same law is proposed as for $k_{I,M1}$ (see Navarro et al., 2017).

3.4 Mechanical behaviour model. Evolution of e_{M2}.

In the stress-strain formulation presented by Navarro et al. (2019), it is assumed that the gas pressure is constant and equal in *M*1 and *M*2. Hence, the same net stress is associated with both *M*1 and *M*2. This constitutive structure and the calculation procedure normally used in DPM was adopted. Therefore, that formulation is also used in the present work, and furthermore, the matric suctions of *M*1 and *M*2, s_{M1} and s_{M2}, respectively, are equal (Eq. [17]: $s_{M1}=P_G-P_{L1}=P_G-P_{L2}=s_{M2}$). Although the stress-strain

model is described in detail in Navarro et al. (2019), its main characteristics are described below, introducing certain simplifications.

Navarro et al. (2019) assume that the macroscopic strain $d\boldsymbol{\varepsilon}$ (engineering or Voigt notation is used throughout the paper for both stress and strain tensors) of the BPM is due to five main processes:

[21] $$d\boldsymbol{\varepsilon} = d\boldsymbol{\varepsilon}^{e}_{M1-s} + d\boldsymbol{\varepsilon}^{p}_{M1-LC} + d\boldsymbol{\varepsilon}_{m} + d\boldsymbol{\varepsilon}_{M1-m} + d\boldsymbol{\varepsilon}^{e}_{M-\sigma}$$

The first two terms introduce the elastic strain caused by $M1$ due to changes in s_M (variable used to define both s_{M1} and s_{M2} in this work), $d\boldsymbol{\varepsilon}^{e}_{M1-s}$, and the plastic strain caused by the rearrangement that occurs in $M1$ when the ellipsoidal generalisation of the load-collapse (LC) yield surface is reached, $d\boldsymbol{\varepsilon}^{p}_{M1-LC}$. Both are modelled using the Barcelona Basic Model (BBM, Alonso et al., 1990).

The third term, $d\boldsymbol{\varepsilon}_{m,}$ defines the strain caused by the rearrangement of the functional level m, which is calculated from the variation of the microstructural void ratio, since its volumetric component, $d\varepsilon_{V,m}$, is given by the expression:

[22] $$d\varepsilon_{V,m} = -\frac{de_m}{1+e}$$

The forth term, $d\boldsymbol{\varepsilon}_{M1-m}$, establishes the deformational coupling between m and $M1$. That is, the strain introduced into the system from the rearrangement caused by $d\boldsymbol{\varepsilon}_m$ in $M1$ even if suction and stress remain constant. It is assumed there are two coupling mechanisms:

[23] $$d\varepsilon_{V,M1-m} = d\varepsilon_{V,M1-m,1} + d\varepsilon_{V,M1-m,2}$$

The first mechanism, $d\varepsilon_{V,M1-m,1}$, describes the changes in packing experienced by $M1$ when the volume of the aggregates changes. To characterise it, the formulation proposed by Sánchez et al. (2005) is adopted, using the Barcelona Expansive Model (BExM, Alonso et al., 1999) as a modelling framework. The second mechanism,

$d\varepsilon_{V,M1-m,2}$, introduces the swelling experienced by *M*1 in the model, as a result of the subdivision of clay particles (Saiyouri et al., 2004) and clay aggregates (Salles et al., 2009) under low confinement conditions. For the macroscopic modelling of this mechanism, the use of the formulation presented by Navarro et al. (2017) is proposed. The fifth term, $d\boldsymbol{\varepsilon}^{e}_{M-\sigma}$, incorporates the strain experienced by the system when the constitutive stress changes. As previously indicated, since both *M*1 and *M*2 have the same gas pressure, both macrostructural levels have the same net stress $\boldsymbol{\sigma}$ ($=\boldsymbol{\sigma}_{TOT}-P_G\cdot\mathbf{m}$, where $\boldsymbol{\sigma}_{TOT}$ is the total stress vector and **m** is the vector form of the Kronecker delta), which is adopted as constitutive stress. Hence, according to Navarro et al. (2019), the term integrates both the effect of *M*1 and *M*2:

[24] $$d\boldsymbol{\varepsilon}^{e}_{M-\sigma} = d\boldsymbol{\varepsilon}^{e}_{M1-\sigma} + d\boldsymbol{\varepsilon}_{M2-\sigma} = \left(\mathbf{C}^{e}_{M1} + \mathbf{C}^{e}_{M2}\right)\cdot d\boldsymbol{\sigma} = \left(\mathbf{D}^{e}_{M}\right)^{-1}\cdot d\boldsymbol{\sigma}$$

where $\mathbf{D}^{e}_{M}$ is the elastic matric of the entire system, calculated from the compliance matrices $\mathbf{C}^{e}_{Mi}$ (i=1, 2), which, in terms of the volumetric and deviatoric strains (using the mean net stress and the von Mises deviatoric stress as conjugated stresses), is defined in axisymmetric problems as:

[25] $$\mathbf{C}^{e}_{Mi} = \begin{bmatrix} 1/K_{Mi} & 0 \\ 0 & 1/3G_{Mi} \end{bmatrix}$$

where K_{Mi} and G_{Mi} are, respectively, the bulk and shear moduli. For simplicity purposes, the Poisson´s ratio is assumed to be constant and equal at both macrostructural levels, $\nu_{M1}=\nu_{M2}=\nu$ (Table 1), defining the shear modulus as:

[26] $$G_{Mi} = \frac{3(1-2\nu)}{2(1+\nu)}K_{Mi}$$

To simplify the calculation of e_{M2}, it is assumed that not only the elastic stiffness of *M*1 for changes in net mean stress, κ_{M1-p}, is constant, but also, that of *M*2, κ_{M2-p} (considered

variable in Navarro et al., 2019), adopting the values in Table 1. Based on these parameters, the values of bulk moduli are calculated as:

$$[27] \qquad K_{\mathrm{Mi-p}} = \frac{(1+e)\,p}{\kappa_{\mathrm{Mi-p}}}$$

Table 1. Hydraulic, mass-transfer and macrostructural stress-strain parameters.

Parameter	Definition	Value
b_1	Material parameter of the intrinsic permeability $k_{\mathrm{I,M1}}$	9.91 [a]
$C_{\mathrm{m\text{-}M1}}$	Constitutive parameter of the mass exchange $r_{\mathrm{M1\text{-}m}}$	0.4 [b]
$H_{\mathrm{m\text{-}M1}}$, $(\mathrm{kPa\cdot s})^{-1}$	Constitutive parameter of the mass exchange $r_{\mathrm{M1\text{-}m}}$	1.5×10^{-8} [b]
$H_{\mathrm{M2\text{-}M1}}$, $(\mathrm{kPa\cdot s})^{-1}$	Constitutive parameter of the mass exchange $r_{\mathrm{M2\text{-}M1}}$	1.0×10^{-11} [c]
k_{O1}, m^2	Reference intrinsic permeability, *M*1	2.34×10^{-21} [a]
m_1	Parameter of the water retention curve, *M*1	0.733 [a]
$s_{\mathrm{A,M2}}$, kPa	Parameter of the water retention curve, *M*2	0.5 [d]
α_1, kPa^{-1}	Parameter of the water retention curve, *M*1	1.15×10^{-4} [a]
λ	Parameter of the water retention curve, *M*2	1.1 [d]
ϕ_{O1}	Reference porosity associated with k_{O1}, *M*1	0.047 [a]
ϕ_{O}	Reference porosity associated with k_{O}, *M*. Test 2	0.319
k	Increase in cohesion with suction	0.1 [a]
p_{C}, kPa	Reference net mean yield stress, BBM in *M*1	10 [a]
r	Soil compressibility parameter, BBM in *M*1	0.8 [a]
β, kPa^{-1}	Soil compressibility parameter, BBM in *M*1	2.0×10^{-5} [a]
$\kappa_{\mathrm{M\text{-}s}}$	Elastic stiffness for changes in suction, *M*	0.001
$\kappa_{\mathrm{M1\text{-}p}}$	Elastic stiffness for changes in net mean stress, *M*1	0.1 [a]

$\kappa_{M1\text{-}s}$	Elastic stiffness for changes in suction, *M*1	0.05 [a]
$\kappa_{M2\text{-}p}$	Elastic stiffness for changes in net mean stress, *M*2	0.7
$\lambda(0)$	Slope of the saturated virgin compression curve, *M*1	0.3 [e]
μ	Slope of the critical state line, BBM in *M*1	1.07 [a]
ν_{M1}	Poisson's ratio, *M*1	0.35 [a]
ν_{M2}	Poisson's ratio, *M*2	0.35 [a]

[a] Data from Navarro et al. (2017). [b] Data from Navarro et al. (2015). [c] Data adapted from Gens et al. (2011). [d] Data adapted from Benson et al. (2014). [e] Data from Toprak et al. (2019).

The definition of a single constitutive stress and a single elastic matrix for the entire system (Eq. [24]) permits the application of an integration procedure of the stress-strain constitutive model which is similar to that implemented when using a DPM (see Sánchez et al., 2005, for instance). In addition, in the numerical solvers used to carry out these integrations, it will be easy to incorporate the calculation of e_{M2} assuming a constant κ_{M2-p}. Therefore, as indicated when analysing the water mass balance in the previous subsection, the incorporation of the D2TPM to a numerical solver initially developed for a DPM will not be a complicated process.

4. HM simulation exercises. Results and discussion

Since the first two tests described in Section 2 were simulated by Navarro et al. (2019) using a PTPM and a DPM, their analyses will permit comparison of the D2TPM with both type of formulations. The first test was carried out with a BPM significantly close (initial average dry density of the sample, 1520 kg/m^3), whereas the second was more open (initial average dry density of the sample equal to 953 kg/m^3). Therefore, the

comparison will permit the illustration of the scope of the new model both when the requirement is not excessive (Test 1, with a low initial value of the inter-pellet void ratio of 0.363; Navarro et al., 2019), and when e_{M2} is high and it is decisive to determine how its value is modelled (Test 2, with an initial inter-pellet void ratio slightly higher than 1; Navarro et al., 2019).

In Test 1, carried out by CEA (France) (Bernachy-Barbe et al., in prep.), in addition to hydraulic data to describe the hydration process, the axial and radial stresses evolution at heights of 60 and 80 mm were also measured. In the simulations, the material parameters presented in Table 1 were assumed. As seen in Fig. 2, the simulation of the stress evolution obtained with the D2TPM was very similar to that obtained using the PTPM, giving both models a prediction of the time evolution that is closer to the experimental data than that of DPM, even after modifying the elastic stiffness for changes in suction of Table 1, using 0.001 for the DPM. With that $\kappa_{M\text{-}s}$, the final values predicted by the three models were similar. The predictions of the time evolution of the water inflow of the three models were also similar (Fig. 3). As shown in Fig.4, since it was a close BPM, the swelling of the microstructure caused the value of e_{M2} to quickly approach zero in the entire sample. Therefore, as illustrated in Fig. 5, the values of P_{L2} and P_{L1} obtained in the PTPM, and the value of P_L calculated with the DPM were quite similar, making their behaviour with respect to flow (Sr_M and $k_{I,M}$) also similar. This led to a similarity of the results obtained with the three models, as contrasted in Figs. 6 a and 6 b, where the experimental and numerical values of the dry density and water content at the end of the test are compared.

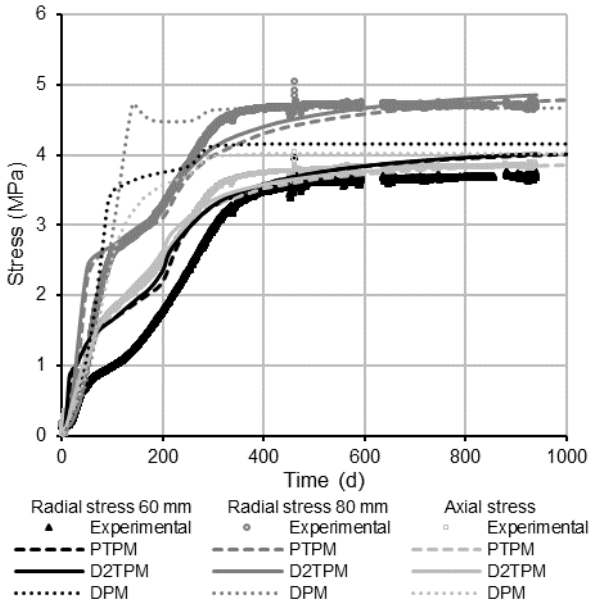

Fig. 2. Time evolution of axial stress and radial stress at heights of 60 and 80 mm in Test 1.

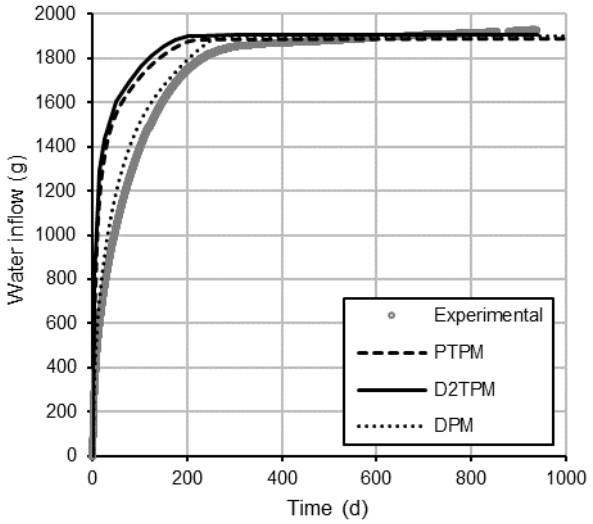

Fig. 3. Water inflow in Test 1.

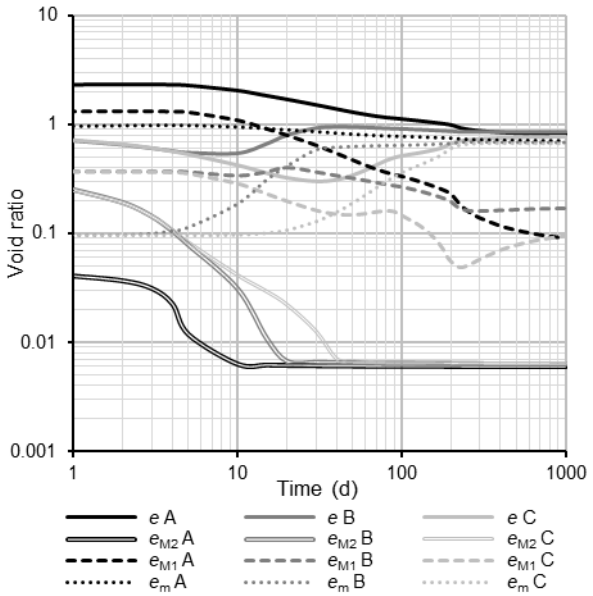

Fig. 4. Test 1. Computed evolution of the void ratios with time at the bottom (A), centre (B) and top (C) of the sample obtained in the PTPM.

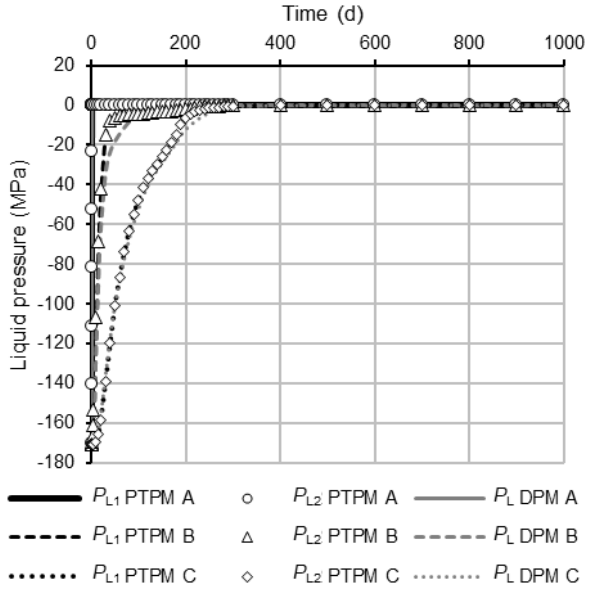

Fig. 5. Test 1. Evolution of P_{L2} and P_{L1} obtained with the PTPM, and P_L calculated using the DPM, at the bottom (A), centre (B) and top (C) of the sample.

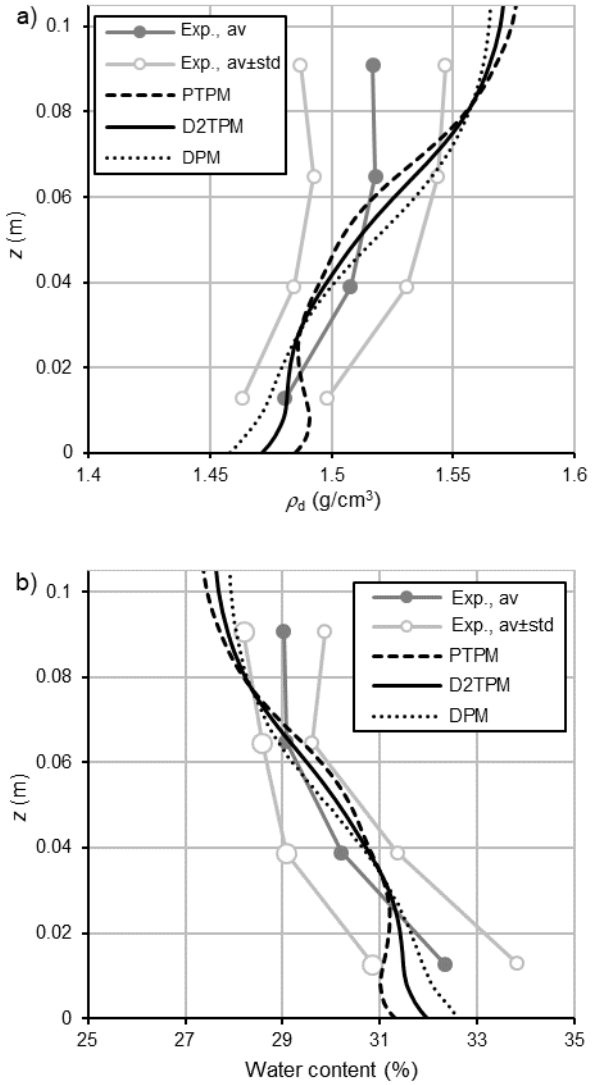

Fig. 6. Test 1, final distribution of dry density (a) and water content (b).

However, in Test 2, this behaviour was not observed. In this test (Åkesson et al., in prep.), the initial average dry density of the sample was equal to 953 kg/m^3, significantly lower than the 1520 kg/m^3 of Test 1. Since the initial value of e_{M2} was very high (close to 1, while in Test 1, it was 0.363), e_{M2} remained high throughout the test, as shown in Fig. 7.

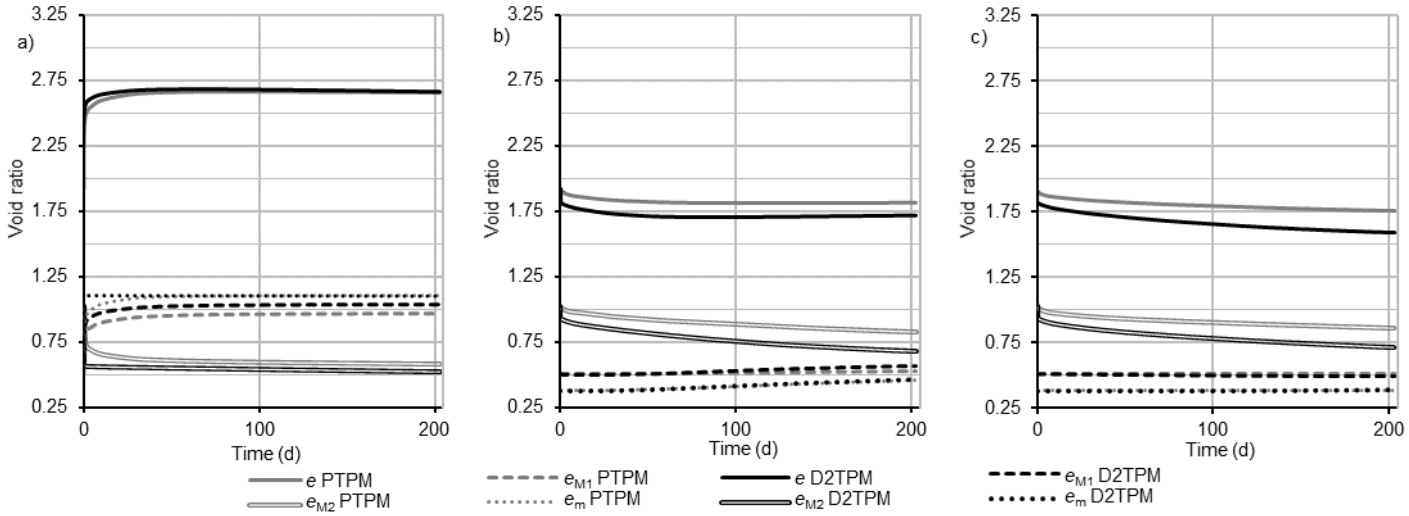

Fig. 7. Evolution of the void ratio during Test 2 at (a) bottom, (b) centre and (c) top of the sample.

This distorts the weighted values of the degree of saturation and permeability, making the value of P_L obtained with the DPM (Fig. 8) different from that obtained with the TPM in the area where the hydration advances. However, the high value of e_{M2} made the degree of saturation of *M*2 low enough for its relative permeability to be negligible, with the flow kinetics being controlled mainly by *M*1. Therefore, the values of P_{L1} and P_{L2} obtained with the PTPM were very similar (Fig. 8), with Eq. [17] being valid, and making the result of D2TPM almost equal to that of PTPM. This is shown in Fig. 9, which represents the experimental and numerical evolution of the relative humidity in three points along of the sample, at 3, 8 and 15.5 cm respectively from the bottom (s1, s2 and s3 sensors). It should be noted that in order to improve the results of the DPM, in addition to modifying the elastic stiffness for changes in suction of Table 1, as done when simulating Test 1 ($\kappa_{M\text{-}s}$ equal to 0.001), the reference porosity associated with the intrinsic permeability was also modified. Hence, instead of the value of 0.047 indicated in Table 1, a value of 0.319 was used. Although this change did not lead to the desired quality in the reproduction of the evolution of liquid pressure, Fig. 9, it permit a good

prediction of the water inflow, Fig. 10. This suggests that at times, the ability to reproduce integrated behaviours does not ensure that the characterisation of the distributed behaviour is sufficiently good. In addition, the examples presented suggest the need to change the parameters used in a DPM to simulate the behaviour of BPM with different structures. On the other hand, if a TPM is adopted, the same conceptual framework (state functions and material parameters) allows to characterise the behaviour of different structures. This is especially interesting if it can be used in D2TPM, since only the value of two new parameters, $s_{A,M2}$ and $\kappa_{M2\text{-}p}$, must be defined with respect to the twenty parameters used in a DPM. The introduction of these two parameters allows to simulate the evolution of e_{M2} (Fig. 7). Thus, as observed in Fig. 11, which shows the distribution of water at the end of Test 2, the distributed behaviour of the system can be satisfactorily characterised.

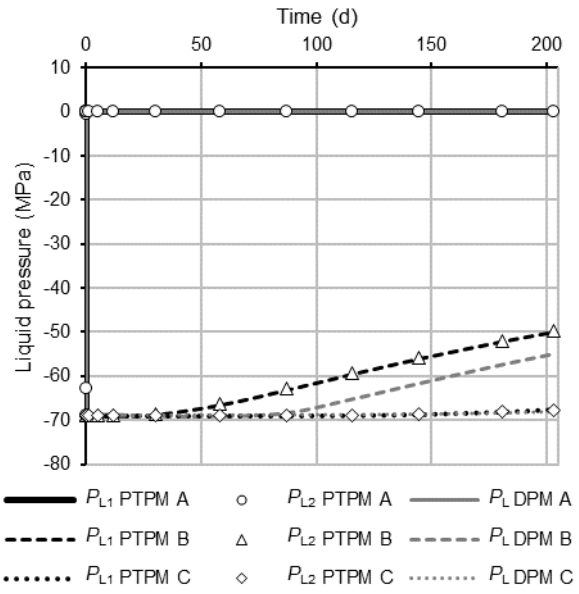

Fig. 8. Test 2. Values of P_{L1} and P_{L2} obtained with the PTPM, and values of P_L obtained with the DPM, at the bottom (A), centre (B) and top (C) of the sample.

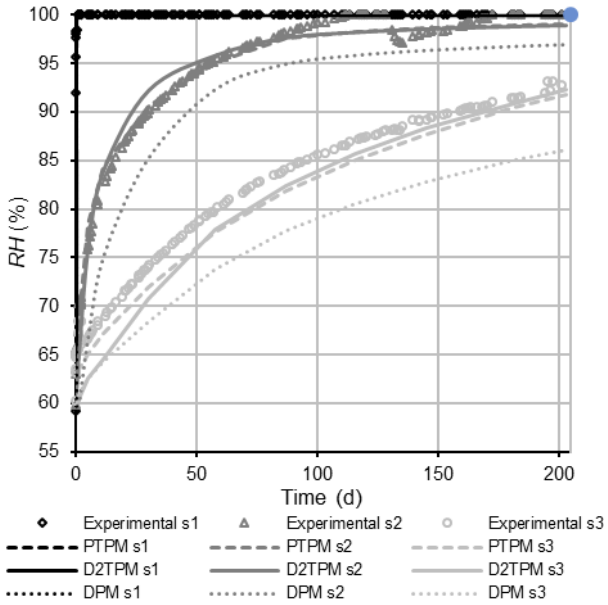

Fig. 9. Test 2. Relative humidity evolution in three points along of the sample, each located at 3 (sensor s1), 8 (sensor s2) and 15.5 cm (sensor s3) respectively from the bottom.

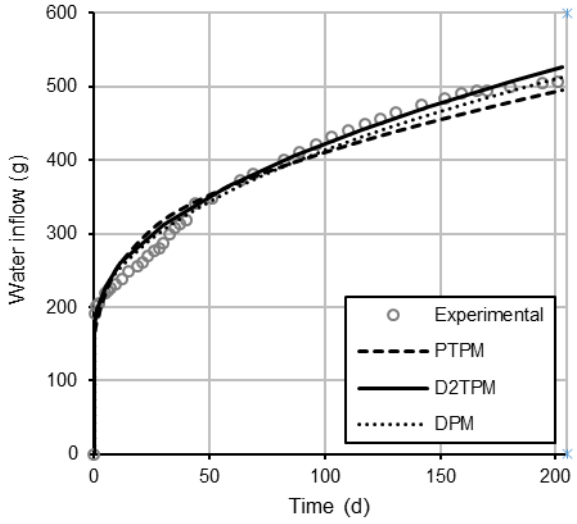

Fig. 10. Test 2. Water inflow.

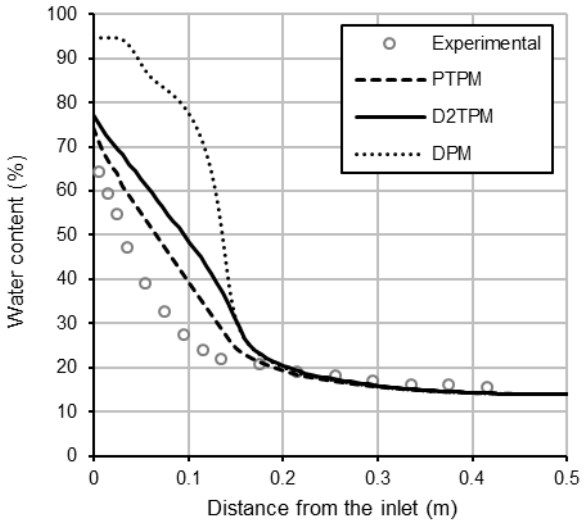

Fig. 11. Distribution of water content at the end of Test 2.

Finally, as an inspection exercise to contrast the capacity of D2TPM, Test 3, carried out by Posiva (Talandier, 2018) was simulated. This is a very demanding exercise, since the behaviours of a BPM and a bentonite block were simulated using a single constitutive framework and the same material parameters for $M1$ in both systems (Table 1) (in blocks, $M2$ is null).

In the test, load cells were placed at the top and bottom of the sample, from which it was observed that the axial stress on the block base (bottom) was different from the one on the top of the pellets (see experimental results in Fig. 12). The difference was due to the effect of the side friction, introduced in the model by a friction that was proportional to the normal stress in the contact between the soil (pellets and block) and the steel of the test cell. A different friction angle for the pellets and block was assumed, Fig. 13. The values of the friction angle, deduced from the values of axial (Fig. 12) and radial (Fig. 14) stresses measured during the test, were consistent with those obtained by Dueck et al. (2016) for MX-80 bentonites.

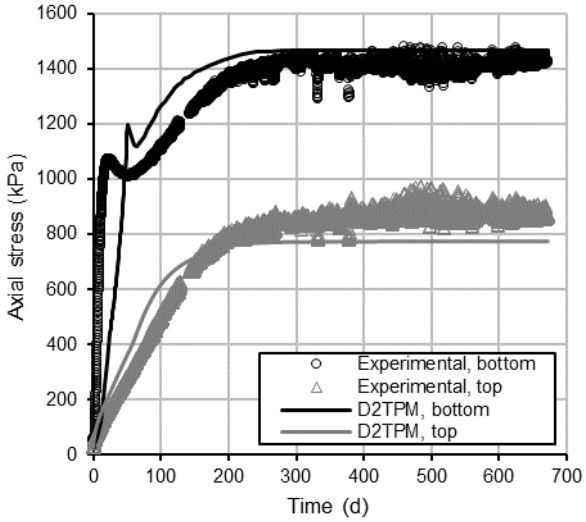

Fig. 12. Evolution of the axial stresses in Test 3

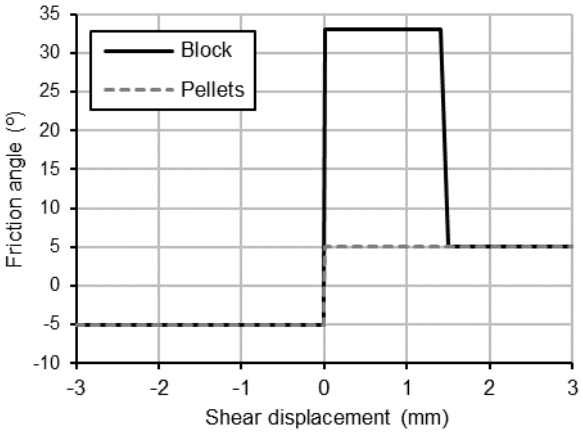

Fig. 13. Variation of the friction angle with the shear displacement in Test 3.

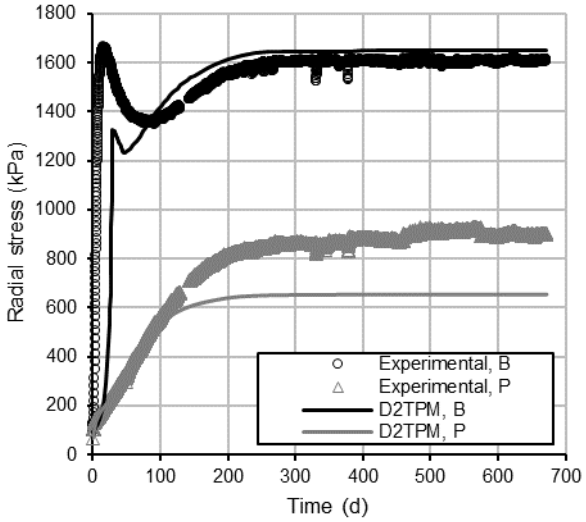

Fig. 14. Radial stresses measured in Test 3. P, pellet load cell, B, block load cell.

As shown in Figs. 12 and 14, the D2TPM allows to obtain good predictions, reproducing not only the difference in axial stress between pellets and block, but also the peaks that occur both in axial and radial stresses measured in sensors located 25 mm from the bottom (block) and the top (pellets). In addition, the final distribution of dry density and water content were also correctly modelled, Figs. 15 a and 15 b, respectively. Overall, simulating this test is a demanding exercise for the model, and thus these results give confidence to the consistency and versatility of D2TPM.

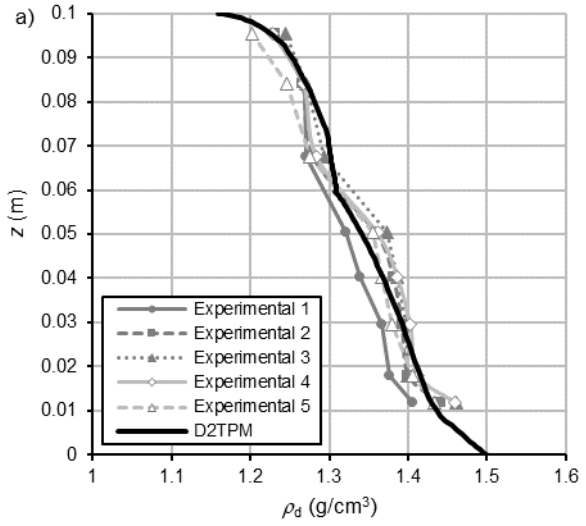

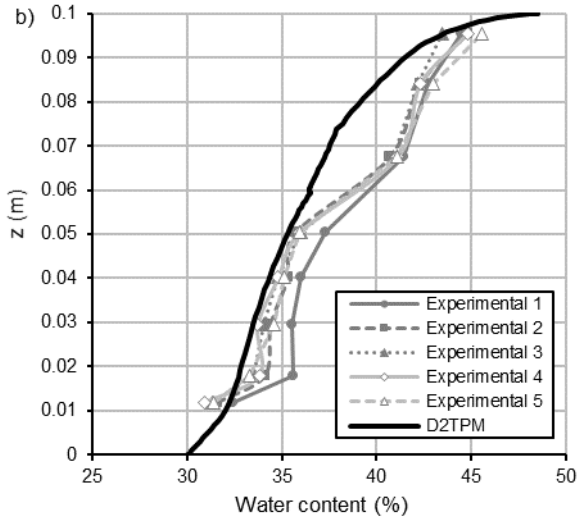

Fig. 15. Final dry density (a) and water content (b) at the end of Test 3.

5. Conclusions

In this work, the hydro-mechanical behaviour of bentonite pellet mixtures (BPM) was analysed. Given the multiporous nature of these materials, macroscopic models based on overlapping continua approaches were used. In the analysis, a pellet triple porosity model (PTPM) was used as reference, with three functional levels being considered to model the effect of inter-pellet space (level *M*2 or macrostructural 2), intra-pellet void space between the clay aggregates (level *M*1, macrostructural 1), and intra-aggregate space (level *m*, microstructural) on the global behaviour of the system, respectively.

The PTPM showed that, if a double porosity model (DPM) is used, some of the magnitudes needed to model the behaviour of BPM are an average of the state functions of PTPM, and are not state functions themselves. Therefore, the assumption that they respond to constitutive models based on material parameters and state variables may be questionable.

However, if the water pressure in *M*1 is equal to that of *M*2, and the gas pressure can be assumed to be constant (in this paper it was assumed to equal the atmospheric pressure), *M*1 and *M*2 have the same suction, being also equal the net stresses at both functional

levels. It is shown that this allows for the adoption of a constitutive formulation to define the deformational behaviour of the macrostructure as a whole, as in a DPM. Consequently, the modification of a calculation procedure based on a double porosity model to incorporate this merged constitutive formulation is not a complicated process. If, in addition, the calculation of the macrostructural water mass and mass flow rate are replaced by the sum of masses and flow rates associated with $M1$ and $M2$, the double porosity calculation procedure will be extended to a conceptual triple porosity model (the new model is referred to as "D2TPM", double to triple porosity model), in which the state functions have a more clearly defined physical meaning.

To facilitate the extension of the DPM to the D2TPM, a simplified model of $M2$ behaviour was proposed. Thus, the intrinsic permeability was calculated with the same formulation and parameters as those used to obtain those of $M1$, assuming that both the degree of saturation and the relative permeability of $M2$ followed a smoothed Heaviside function. To characterise the deformability of $M2$, a log-linear elastic model was used. Therefore, only two new constitutive parameters are introduced.

Despite its simplicity, the proposed formulation allowed to obtain good results both when simulating the behaviour of an open BPM, and when reproducing the behaviour of a closed mixture. In both cases, the quality of the obtained predictions with the D2TPM were comparable to those obtained with the PTPM, improving the prediction capacity of a DPM. This seems to confirm the greater consistency (physical meaning) of the state functions used in triple porosity models. In addition, the results are good, even when simulating the swelling of a bentonite block and a BPM using the same material parameters to model the behaviour of the macrostructural level $M1$ in both materials. These results give confidence to the D2TPM. Therefore, given the relative simplicity

with which it can be implemented from DPM, it constitutes a tool to be considered to improve the characterisation of BPM behaviour.

Acknowledgements

This study was funded in part by Posiva Oy project 2113799, by FPU Grant FPU15/02655 from the Spanish Ministry of Education awarded to Ms. De la Morena and by Beacon project, which receives funding from the Euratom research and training programme 2014-2018 under grant agreement No 745942. In addition, we would like to thank Clay Technology, CEA and Posiva for allowing us to use the results of their experimental work.

References

Åkesson, M., Goudarzi, R., Börgesson, L., In prep. EBS TF – THM Modelling. Water transport in pellets-filled slots. Laboratory tests and task descriptions. SKB P-19-06. Svensk Kärnbränslehantering AB, Swedish Nuclear Fuel and Waste Management Co.

Alonso, E.E., Gens, A., Josa, A., 1990. A constitutive model for partially saturated soils. Géotechnique 40(3), 405-430. https://doi.org/10.1680/geot.1990.40.3.405.

Alonso, E.E., Romero, E., Hoffmann, C., 2011. Hydromechanical behaviour of compacted granular expansive mixtures: Experimental and constitutive study. Géotechnique 61(4), 329-344. https://doi.org/10.1680/geot.2011.61.4.329.

Alonso, E.E., Vaunat, J., Gens, A. 1999. Modelling the mechanical behaviour of expansive clays. Eng. Geol. 54(1-2), 173-183. https://doi.org/10.1016/S0013-7952(99)00079-4.

Barenblatt, G.I., Zheltov, I.P., Kochina, I.N., 1960. Basic concepts in the theory of seepage of homogeneous liquids in fissured rocks [strata]. J. Appl. Math. Mech. 24(5), 1286-1303. https://doi.org/10.1016/0021-8928(60)90107-6.

Benson, C.H., Chiang, I., Chalermyanont, T., Sawangsuriya, A., 2014. Estimating van genuchten parameters α and n for clean sands from particle size distribution data. Geotech. Spec. Publ. 233, 410-427. https://doi.org/10.1061/9780784413265.033.

Bernachy-Barbe, F., Imbert, C., Conil, N., Guillot, W., Gatabin, C., Talandier, J., In prep. Heterogeneities in the final state of MX-80 bentonite under granular form in laboratory scale resaturation tests.

Bian, X., Cui, Y.J., Li, X.Z., 2019. Voids effect on the swelling behaviour of compacted bentonite. Géotechnique 69(7), 593-605. https://doi.org/10.1680/jgeot.17.P.283.

Dueck, A., Goudarzi, R., Börgesson, L., 2016. Buffer homogenisation. Status report 3. SKB Technical Report TR-16-04. Svensk Kärnbränslehantering AB, Swedish Nuclear Fuel and Waste Management Co. http://www.skb.com/publication/2485340/TR-16-04.pdf (accessed November 2019).

Edlefsen, N.E., Anderson, A.B.C., 1943. Thermodynamics of soil moisture. Hilgardia 15(2), 31-298. https://doi.org/10.3733/hilg.v15n02p031.

García-Siñeriz, J.L., Villar, M.V., Rey, M., Palacios, B., 2015. Engineered barrier of bentonite pellets and compacted blocks: State after reaching saturation. Eng. Geol. 192, 33-45. https://doi.org/10.1016/j.enggeo.2015.04.002.

Gens, A., Alonso, E.E., 1992. A framework for the behaviour of unsaturated expansive clays. Can. Geotech. J. 29(6), 1013-1032. https://doi.org/10.1139/t92-120.

Gens, A., Valleján, B., Sánchez, M., Imbert, C., Villar, M.V., van Geet, M., 2011. Hydromechanical behaviour of a heterogeneous compacted soil: Experimental observations and modelling. Géotechnique 61(5), 367-386. https://doi.org/10.1680/geot.SIP11.P.015.

Guimarães, L.D.N., Gens, A., Sánchez, M., Olivella, S., 2013. A chemo-mechanical constitutive model accounting for cation exchange in expansive clays. Géotechnique 63(3), 221-234. https://doi.org/10.1680/geot.SIP13.P.012.

Hoffmann, C., Alonso, E.E., Romero, E., 2007. Hydro-mechanical behaviour of bentonite pellet mixtures. Phys. Chem. Earth 32(8-14), 832-849 https://doi.org/10.1016/j.pce.2006.04.037.

Imbert, C., Villar, M.V., 2006. Hydro-mechanical response of a bentonite pellets/powder mixture upon infiltration. Appl. Clay Sci. 32(3-4), 197-209. https://doi.org/10.1016/j.clay.2006.01.005.

Karnland, O., Nilsson, U., Weber, H., Wersin, P., 2008. Sealing ability of Wyoming bentonite pellets foreseen as buffer material - Laboratory results. Phys. Chem. Earth 33(SUPPL. 1), S472-S475. https://doi.org/10.1016/j.pce.2008.10.024.

Karnland, O., Olsson, S., Nilsson, U., 2006. Mineralogy and sealing properties of various bentonites and smectite-rich clay materials. SKB Technical Report TR-06-30. Svensk Kärnbränslehantering AB, Swedish Nuclear Fuel and Waste Management Co. http://www.skb.com/publication/1419144/TR-06-30.pdf (accessed November 2019).

Khalili, N., Valliappan, S., Wan, C.F., 1999. Consolidation of fissured clays. Géotechnique 49(1), 75-89. https://doi.org/10.1680/geot.1999.49.1.75.

Kiviranta, L., Kumpulainen, S., 2011. Quality control and characterization of bentonite materials. Posiva Working Report 2011-84. Posiva Oy. http://www.posiva.fi/files/1994/WR_2011-84_web.pdf (accessed November 2019).

Kiviranta, L., Kumpulainen, S., Pintado, X., Karttunen, P., Schatz, T., 2018. Characterization of Bentonite and Clay Materials 2012-2015-. Posiva Working Report 2016-05. Posiva Oy. http://www.posiva.fi/files/4904/WR_2016-05_web.pdf (accessed November 2019).

Lloret, A., Villar, M.V., 2007. Advances on the knowledge of the thermo-hydro-mechanical behaviour of heavily compacted "FEBEX" bentonite. Phys. Chem. Earth 32(8-14), 701-715. https://doi.org/10.1016/j.pce.2006.03.002.

Lloret, A., Villar, M.V., Sánchez, M., Gens, A., Pintado, X., Alonso, E.E., 2003. Mechanical behaviour of heavily compacted bentonite under high suction changes. Géotechnique 53(1), 27-40. https://doi.org/10.1680/geot.53.1.27.37258.

Luterkort, D., Johannesson, L.E., Eriksson, P., 2017. Buffer design and installation method. Installation report. SKB Technical Report TR-17-06. Svensk Kärnbränslehantering AB, Swedish Nuclear Fuel and Waste Management Co. http://www.skb.com/publication/2490718/TR-17-06.pdf (accessed November 2019).

Manca, D., Ferrari, A., Laloui, L., 2016. Fabric evolution and the related swelling behaviour of a sand/bentonite mixture upon hydro-chemo-mechanical loadings. Géotechnique 66(1), 41-57. https://doi.org/10.1680/jgeot.15.P.073.

Mašín, D., 2013. Double structure hydromechanical coupling formalism and a model for unsaturated expansive clays. Eng. Geol. 165, 73-88. https://doi.org/10.1016/j.enggeo.2013.05.026.

Mašín, D., Khalili, N., 2016. Swelling phenomena and effective stress in compacted expansive clays. Can. Geotech. J. 53(1), 134-147. https://doi.org/10.1139/cgj-2014-0479.

Molinero Guerra, A., Cui, Y.J., He, Y., Delage, P., Mokni, N., Tang, A.M., Aimedieu, P., Bornert, M., Bernier, F., 2019. Characterization of water retention, compressibility and swelling properties of a pellet/powder bentonite mixture. Eng. Geol. 248, 14-21. https://doi.org/10.1016/j.enggeo.2018.11.005.

Molinero Guerra, A., Cui, Y.J., Mokni, N., Delage, P., Bornert, M., Aimedieu, P., Tang, A.M., Bernier, F., 2018. Investigation of the hydro-mechanical behaviour of a pellet/powder MX80 bentonite mixture using an infiltration column. Eng. Geol. 243, 18-25. https://doi.org/10.1016/j.enggeo.2018.06.006.

Molinero Guerra, A., Mokni, N., Delage, P., Cui, Y.J., Tang, A.M., Aimedieu, P., Bernier, F., Bornert, M., 2017. In-depth characterisation of a mixture composed of powder/pellets MX80 bentonite. Appl. Clay Sci. 135, 538-546. https://doi.org/10.1016/j.clay.2016.10.030.

Musso, G., Romero, E., Gens, A., Castellanos, E., 2003. The role of structure in the chemically induced deformations of FEBEX bentonite. Appl. Clay Sci. 23(1-4), 229-237. https://doi.org/10.1016/S0169-1317(03)00107-8.

Navarro, V., Asensio, L., De la Morena, G., Pintado, X., Yustres, Á., 2015. Differentiated intra-and inter-aggregate water content models of mx-80 bentonite. Appl. Clay Sci. 118, 325-336. https://doi.org/10.1016/j.clay.2015.10.015.

Navarro, V., Asensio, L., Gharbieh, H., De la Morena, G., Pulkkanen, V.M., 2019. A triple porosity hydro-mechanical model for MX-80 bentonite pellet mixtures. Eng. Geol. In Press. https://doi.org/10.1016/j.enggeo.2019.105311.

Navarro, V., Yustres, Á., Asensio, L., De la Morena, G., González-Arteaga, J., Laurila, T., Pintado, X., 2017. Modelling of compacted bentonite swelling accounting for salinity effects. Eng. Geol. 223, 48-58. https://doi.org/10.1016/j.enggeo.2017.04.016.

Nowamooz, H., Mrad, M., Abdallah, A., Masrouri, F., 2009. Experimental and numerical studies of the hydromechanical behaviour of a natural unsaturated swelling soil. Can. Geotech. J. 46(4), 393-410. https://doi.org/10.1139/T08-127.

Pollock, D.W., 1986. Simulation of Fluid Flow and Energy Transport Processes Associated With High-Level Radioactive Waste Disposal in Unsaturated Alluvium. Water Resour. Res. 22(5), 765-775. https://doi.org/10.1029/WR022i005p00765.

Saiyouri, N., Tessier, D., Hicher, P.Y., 2004. Experimental study of swelling in unsaturated compacted clays. Clay Miner. 39(4), 469-479. https://doi.org/10.1180/0009855043940148.

Salles, F., Douillard, J.M., Denoyel, R., Bildstein, O., Jullien, M., Beurroies, I., Van Damme, H., 2009. Hydration sequence of swelling clays: Evolutions of specific surface area and hydration energy. J. Colloid Interface Sci. 333(2), 510-522. https://doi.org/10.1016/j.jcis.2009.02.018.

Sánchez, M., Gens, A., Guimarães, L.D.N., Olivella, S., 2005. A double structure generalized plasticity model for expansive materials. Int. J. Numer. Anal. Method. Geomech. 29(8), 751-787. https://doi.org/10.1002/nag.434.

Sánchez, M., Gens, A., Villar, M.V., Olivella, S., 2016. Fully coupled thermo-hydro-mechanical double-porosity formulation for unsaturated soils. Int. J. Geomech. 16(6). https://doi.org/10.1061/(ASCE)GM.1943-5622.0000728.

Sellin, P., Leupin, O.X., 2013. The use of clay as an engineered barrier in radioactive-waste management - A review. Clay. Clay Miner. 61(6), 477-498. https://doi.org/10.1346/CCMN.2013.0610601.

Talandier, J., 2018. Specifications for Beacon WP5: Testing, verification and validation of models. Step 1- Verification cases. Deliverable D5.1.1 for BEACON project. https://ec.europa.eu/research/participants/documents/downloadPublic?documentIds=080166e5c1408929&appId=PPGMS (accessed November 2019).

Toprak, E., Olivella, S., Pintado, X., 2019. Modelling engineered barriers for spent nuclear fuel repository using a double-structure model for pellets. Environ. Geotech., In press. https://doi.org/10.1680/jenge.17.00086.

Vilarrasa, V., Rutqvist, J., Blanco Martin, L., Brikholzer, J., 2016. Use of a Dual-Structure Constitutive Model for Predicting the Long-Term Behavior of an Expansive Clay Buffer in a Nuclear Waste Repository. Int. J. Geomech. 16(6), D4015005. https://doi.org/10.1061/(ASCE)GM.1943-5622.0000603.

Wilson, R.K., Aifantis, E.C., 1982. On the theory of consolidation with double porosity. Int. J. Eng. Sci. 20(9), 1009-1035. https://doi.org/10.1016/0020-7225(82)90036-2.

Yong, R.N., 1999. Overview of modeling of clay microstructure and interactions for prediction of waste isolation barrier performance. Eng. Geol. 54(1-2), 83-91. https://doi.org/10.1016/S0013-7952(99)00064-2.